Computational Materials Science 161 (2019) 135–142

Contents lists available at ScienceDirect

Computational Materials Science

journal homepage: www.elsevier.com/locate/commatsci

A fully molecular dynamics-based method for modeling nanoporous gold

Maxime Guillotte*, Julien Godet, Laurent Pizzagalli

Department of Physics and Mechanics of Materials, Institut Pprime, CNRS-Université de Poitiers UPR 3346, SP2MI, BP 30179, F-86962 Futuroscope Chasseneuil Cedex, France

ARTICLE INFO

Keywords:
Nanoporous gold
Molecular dynamics
Model
Structure
Elasticity

ABSTRACT

Models that can be used to describe nanoporous gold are often generated either by phase-field or Monte-Carlo methods. It is not ascertained that these models are closely matching experimental systems, and there is a need for other variants. Here is proposed an original approach to generate alternative models, which is solely based on molecular dynamics simulations. Structures obtained with this method are structurally characterized by determining the ligaments diameter distributions, the scaled genus densities and the interfacial shape distributions. Selected mechanical characterizations are also done by deforming the structures in tension and in compression. Structural and mechanical properties are in good agreement with experimental and theoretical published results.

1. Introduction

Sponge-like nanoporous gold (NPG) is a nano-architectured free-standing material resulting from the self-organization of gold after the selective dissolution of silver in a AuAg alloy. NPG can be potentially useful in various fields such as catalysis [1] (due to its high specific surface area and to its atomic sized defects created by the curvature of ligaments), detection of biomolecules [2,3] (due to its high conductivity and good biocompatibility) and of neural activity in noisy environments [4], or as photosystems [5,6]. In addition to being potentially functionalized, NPG has the interesting property of being both light and resistant. However, some of its characteristics remain poorly understood [7]. For example, the strength and stiffness tend to deviate from the Gibson-Ashby scaling laws [8–10]. Also, gold is known to be a highly ductile material but NPG yields by brittle fracture during tensile tests [11,12]. Hence, it is of great interest to understand the fundamental elementary mechanisms leading to this behavior.

Molecular dynamics (MD) simulations are well-suited for investigating mechanisms at the atomic scale. However, a prerequisite for such simulations is to have realistic models of NPG. These are usually generated using phase-field [8,9,13,14,15], Monte-Carlo [16–19] methods. Phase-field methods are based on numerically solving the Cahn-Hilliard equation to reproduce spinodal decomposition. The dealloying process is then modeled as a diffusion phenomenon at the interface between two phases. Monte-Carlo methods explore multiple configurations of the system and keep the best ones based on thermodynamic considerations. The geometry of NPG models can next be compared to tomographic reconstructions of NPG samples. The latter can be obtained using focused ion beam [20], transmission electron microscope [21] or by transmission X-ray microscope [22,23]. Note that these reconstructed samples can also be used as realistic models of NPG for MD simulations.

To compare NPG models, different structural properties can be used, such as the ligaments diameter distribution and its associated average D_m, the scaled genus density ($\overline{g_v}$) which quantifies the connectivity, and the interfacial shape distribution (ISD) which is the distribution of the local curvature of the ligaments and characterizes the morphology. The structural properties of NPG are highly correlated to mechanical or catalytic properties [1,15,24]. Models can also be compared on the basis of mechanical considerations. The elastic moduli, the strength, the local and global mechanisms of plastic deformation, as well as the mechanisms of rupture are appropriate indicators.

Hereinafter, we present a new method to generate NPG models which is entirely based on molecular dynamics. The purpose of this paper is twofold: first, to describe the method, and second to propose few structural and mechanical characterizations demonstrating the soundness of the generated systems. The method is fully described in Section 2. The following section presents the results of the structural and mechanical characterizations. Finally, the main conclusions are outlined in Section 4.

2. Methods

The MD simulations were run with the open-source code LAMMPS [25]. Periodic boundary conditions have been applied along the three directions of space, and a timestep of 1 fs has been used to assure

* Corresponding author.
E-mail addresses: maxime.guillotte@univ-poitiers.fr (M. Guillotte), julien.godet@univ-poitiers.fr (J. Godet), laurent.pizzagalli@univ-poitiers.fr (L. Pizzagalli).

https://doi.org/10.1016/j.commatsci.2019.01.042
Received 28 September 2018; Received in revised form 22 January 2019; Accepted 25 January 2019
0927-0256/ © 2019 Elsevier B.V. All rights reserved.

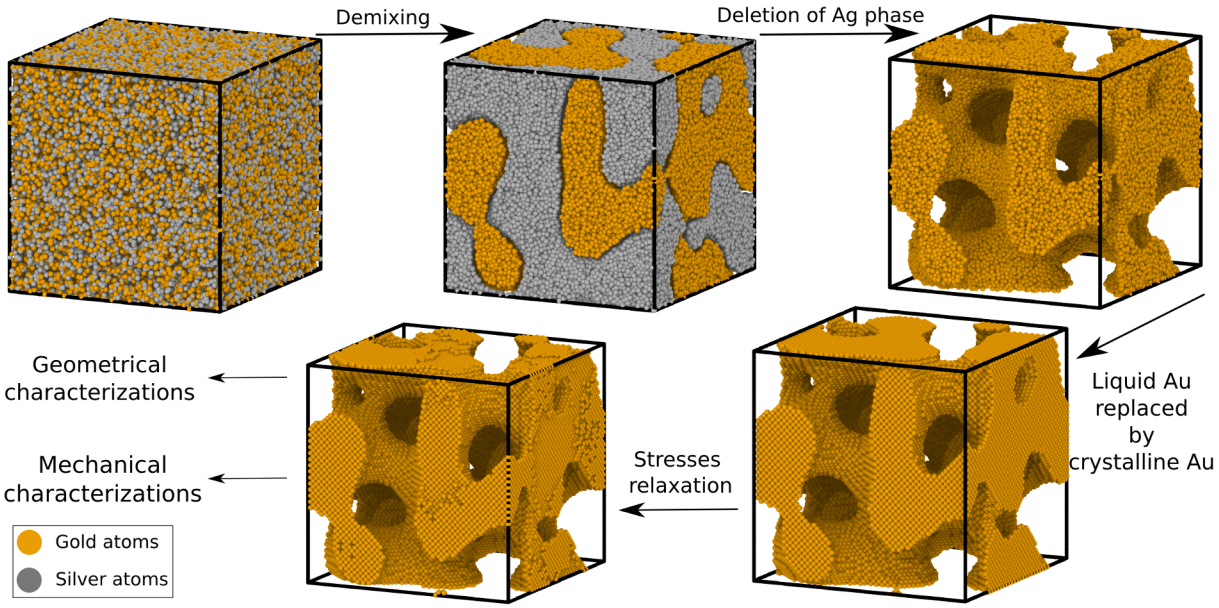

Fig. 1. Graphical summary of the main steps of the procedure.

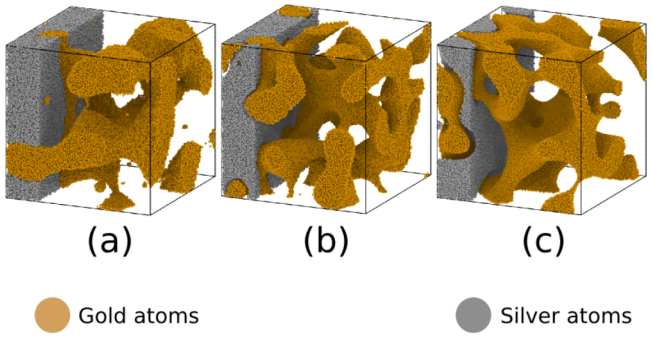

Fig. 2. Influence of the Au-Ag potential parameter σ on the demixing process. A part of silver atoms are removed for clarity. Figures a, b and c are snapshots obtained with σ = 2, 7, and 15 Å and simulation times of 150, 60 and 30 ps, respectively. One can see isolated clusters in (a) and the interfacial void in (c). The temperature of demixing is 1800 K.

integration stability of Newton equations. The different characterizations have been made with the open source software Ovito [26] and the commercial package Avizo.

2.1. General concepts of the method

To illustrate the different steps of the method, one can refer to the Fig. 1. Two different species with defined concentrations are first introduced in the simulation box. Gold and silver are chosen because their melting temperatures are relatively close. Then, a first MD run is performed at a temperature T_d, here equal to 1800 K, higher than the melting point of both elements. By making the Ag and Au phases artificially immiscible (see Section 2.2), the system evolves to form distinct Au and Ag phases, as shown in the Fig. 3. These phases are continuous and their morphologies essentially depend on simulation time, initial concentrations and temperature. Finally, the silver phase is deleted and the liquid gold one is replaced by a crystalline phase using a homemade script detailed in Section 2.5, leading to a monocrystalline NPG.

2.2. Interatomic potentials

In the MD simulations, the Au-Au and Ag-Ag interactions are described by the EAM potentials developed by Foiles et al. [27]. The lattice parameter of Au given by this potential is 4.08 Å. For the Au-Ag interactions, a fully repulsive Lennard-Jones potential is used. Although such a potential is not able to provide a realistic description of the Au-Ag alloy, it is convenient to accelerate the demixing since it makes Au and Ag strictly immiscible. The energy versus the distance between two atoms is given by:

$$E(r) = 4\,\epsilon\left[\left(\frac{\sigma}{r}\right)^{12} - \left(\frac{\sigma}{r}\right)^{6}\right], \quad r < r_c \tag{1}$$

where r is the interatomic distance, σ is the distance at which the energy equals zero, ϵ is a scaling energy parameter and r_c is the cutoff distance (i.e. the distance beyond which two atoms do not interact). In order to have a fully repulsive potential, σ must be equal or higher than r_c. The continuity of the energy as a function of the interatomic distance is ensured by making σ and r_c equal. σ is the most influential parameter. A too low value leads to the formation of atom clusters embedded in the other phase. A too high value prevents cluster formation but creates a significant void region between the two phases. This void may lead to an error in the setting of foam density (detailed in Section 2.3). Besides, the higher is σ, the smoother is the interface. These cases described above are shown in Fig. 2. In the following we chose $\sigma = r_c = 7$ Å (Fig. 2 (b)) and $\epsilon = 0.001$ eV as appropriate values.

2.3. Initial setup

With our method, the relative density ρ can be precisely set. It is defined as the density of the foam over the density of the bulk, and is also equal to the volume of the gold phase V_{Au} over the total volume of the foam V. In addition, we have:

$$N_{Au} = V_{Au} \times \delta_{Au}, \tag{2}$$

where N_{Au} is the number of gold atoms and δ_{Au} is the volumetric atomic density of the gold phase at T_d. δ_{Au} depends on the temperature and is computed by first filling a cubic simulation box of $\simeq 22\,\text{nm}^3$ with fcc gold atoms and next letting the system evolves at the temperature T_d in the NPT ensemble for 100 ps with the EAM Au-Au potential. δ_{Au} is then obtained by dividing the number of Au atoms by the volume of the box. Hence, the number of Au atoms to put in the simulation box for the desired ρ at T_d is:

$$N_{Au} = \rho \times V \times \delta_{Au} \tag{3}$$

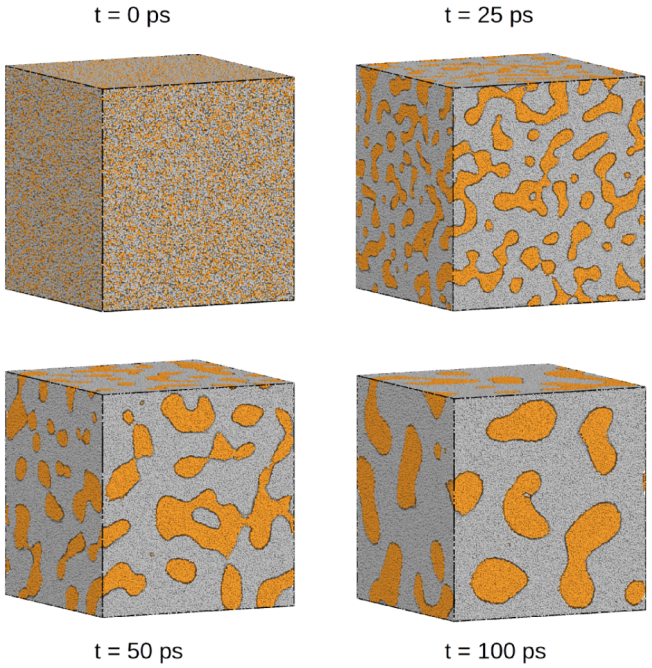

Fig. 3. Demixing of gold (in orange) and silver (in grey) phases at different times during a MD simulation.

By the same line of reasoning, the number of silver atoms to put in the simulation box to fill the remaining volume is:

$$N_{Ag} = (1 - \rho) \times V \times \delta_{Ag} \tag{4}$$

Note that this does not take into account the reduction of gold phase volume due to the relaxation of surface stresses during the stabilization of the upcoming crystalline structure.

2.4. Demixing process

The estimated numbers of gold and silver atoms are next randomly placed in the simulation box, 1000 steps are first performed using the conjugate gradient algorithm to move apart overlapping atoms. Then a MD run is done in the NVT ensemble at T_d and with a temperature damping parameter of 0.05 ps. The gold phase morphology, and in particular the mean diameter D_m of foam ligaments can be monitored during the demixing by computing the specific surface $S_v = S_{Au}/V_{Au}$ of the gold phase with a software like Ovito [26] (where S_{Au} and V_{Au} are the surface area and the volume of the gold phase, respectively). S_v is shown to be inversely proportional to the D_m (Fig. 4), which is determined using the skeletonization method detailed in the Section 3.1). The proportionality coefficient has a weak dependence on ρ and on the parameters used to determine S_v. In Ovito, S_v is obtained by meshing the surface using a virtual probing sphere method [28]. The sphere radius is here set to 5 Å so that the ratio V_{Au}/V is equal to ρ. The duration of the MD run then depends on the desired morphology (controlled by a visual inspection and S_v monitoring). Typically, a mean diameter of $\simeq$ 4 nm is attained after 100 ps with the potentials used in this work (Fig. 4). Once the mean diameter has attained the desired value, the MD simulation is stopped.

The use of the repulsive potential makes gold and silver immiscible, allowing for phase separation thanks to volume diffusion. Then the process resembles spinodal decomposition. However, it is not obvious that the resulting phase separation mechanism is exactly the same to the one modeled by phase field approaches. For instance, it is interesting to note that, being atomistic, our method allows for atomic diffusion at the Ag-Au interface during model generation, leading to gold surface smoothening as in dealloying.

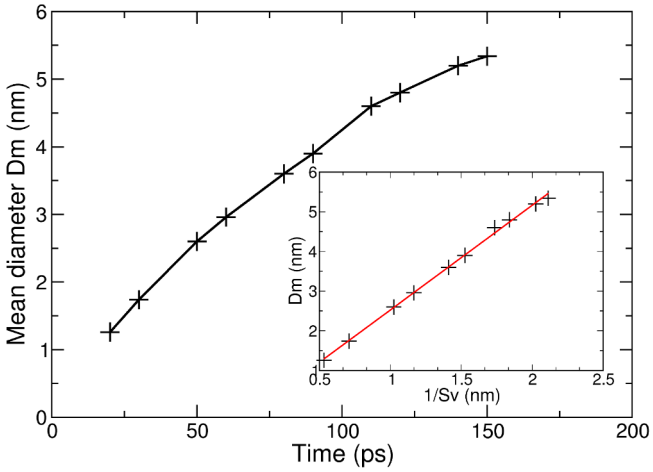

Fig. 4. Evolution of the mean diameter D_m of the ligaments foam as a function of time. The inset shows the linear dependence between D_m and $1/S_v$, S_v being the specific surface.

2.5. From liquid gold to the final NPG model

The liquid silver phase is next entirely deleted. In order to replace the liquid gold phase by a crystalline phase, one can create a surface mesh of the liquid phase and fill this closed surface by a crystalline phase. Some open source codes exist for this purpose (see for example Nanosculpt [29]). We developed a homemade procedure for additional flexibility and potentialities (like creating a polycrystalline foam). In this one, the simulation box that already contains the gold liquid phase is entirely filled with a monocrystalline gold fcc structure. The chosen crystallographic orientations are $\langle 1\,0\,0 \rangle$ in the three principal directions $\hat{x}$, $\hat{y}$ and $\hat{z}$ of the simulation box. We focus here on monocrystalline structures, given the dimensions of MD models [30–32], even if it is possible to generate polycrystalline NPG with this method. Next, logical operations are performed to keep only atoms of the crystalline phase that overlap or are very close to atoms of the liquid phase (with a maximum separation of 3 Å). Finally, the entire liquid phase is deleted.

Afterwards, stresses in the newly created crystalline foam are relaxed according to the following procedure. First, a MD run is performed at 900 K in the NVT ensemble during 0.2 ns. This run allows for a rough relaxation of surface stresses. A second MD run is next performed in the NPT ensemble at 900 K during 1 ns to make pressure vanish on the simulation box. A resulting structure is shown in Fig. 5. Because of the known limitations of MD calculations (number of atoms, time scale) and to preserve a minimum number of ligaments in the simulation box, D_m is kept lower than 7 nm in this work. Diameters for some of the experimental NPG are in this range [33–36].

At this point, we have generated a single crystalline nanoporous gold structure, which is visually similar (see Fig. 5)) to other models reported in the literature [15], or to real samples reconstructed by tomography [23,37].

2.6. MD mechanical tests

A first MD run is performed at 100 K in the NPT ensemble during 0.5 ns for thermalization. For all the compressive and tensile uniaxial deformation tests a constant engineering strain rate of $10^8\,s^{-1}$ is used, as well as damping parameters of 0.1 ps and 1 ps for temperature and pressure control, respectively. The tests are performed by varying the box dimension along $\hat{z}$ and allowing only dimensions along $\hat{x}$ and $\hat{y}$ to relax. The structures are deformed along [100] from 0% to 30% engineering strain, both in tension and in compression. The elastic moduli are calculated by a linear fit of the stress-strain curves for strains ranging from 0% to 2%.

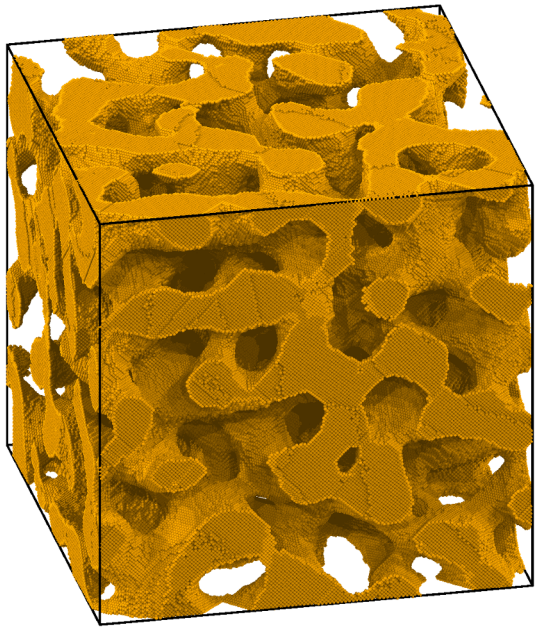

Fig. 5. Example of a NPG model generated using our method, characterized by a relative density $\rho = 0.43$, a total volume $V \simeq 45^3\,nm^3$ and a mean ligament diameter $D_m = 3.7$ nm.

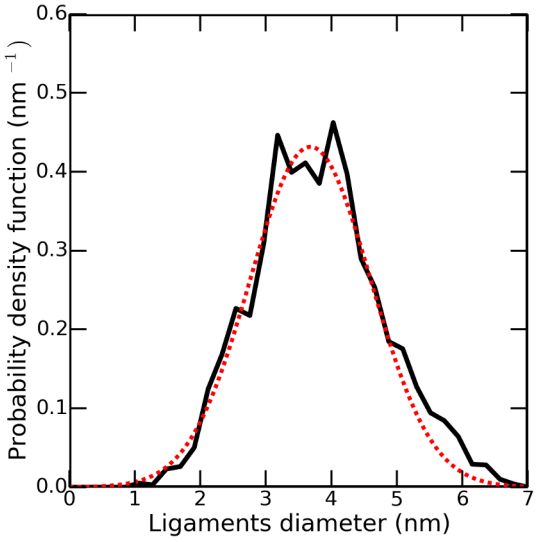

Fig. 6. Ligament diameter distribution for one of our models (black curve) and a fitted normal distribution (red dashed curve). The relative density and mean diameter are 0.43 and 3.7 nm, respectively.

3. Results

The aim of this part is to validate our approach by comparing structural and mechanical characterizations of our models to the state of the art. Results shown in Figs. 6, 8, 10, 12 and 13 are obtained using the same foam model. All other results (that show a dependance on ρ) are obtained with multiple models of different D_m.

3.1. Structural analysis

In this section the relevant structural properties of our NPG models are compared to the literature. The skeletonization method is suitable to compute the mean diameter D_m of the foam ligaments. In this approach [38,39], the volume is thinned until only a one-voxel thick skeleton remains. After thinning, each ligament can be distinguished. At each point of the skeleton, the number of removed voxels allows to determine the local thickness. With this information, the diameter of each ligament and therefore the mean diameter of the foam can be obtained. Fig. 6 shows the probability density function of the ligaments diameter of one of our systems ($\rho = 0.43$, $V \simeq 45^3\,nm^3$ and $D_m = 3.7$ nm). This quantity can be described by a normal distribution for all our models.

A second important property is the scaled genus density:

$$\overline{g_v} = \frac{g}{V} \times S_v^{-3}, \tag{5}$$

where g is the genus of the closed surface, V the total volume of the foam and S_v the specific surface. The genus is calculated as follows: first, the surface mesh is built with millions of triangular faces using the method implemented in Ovito [28], based on the alpha-shape method. Then, one can compute:

$$\chi = V - E + F, \tag{6}$$

where χ is the Euler characteristic, V the number of vertices, E the number of edges and F the number of faces forming the closed surface. Then, the genus is:

$$g = 1 - (\chi/2), \tag{7}$$

A simpler definition of the genus is the number of holes, or handles, made by the closed surface. For example, a sphere, a torus and a double torus have a genus $g = 0$, $g = 1$ and $g = 2$, respectively. Hence, the genus is representative of the connectivity (the topology) of the foam. But this quantity is not convenient for comparing systems whose volume or mean diameter are different. This is why the genus is usually normalized by the total volume of the foam and made dimensionless by the cubed characteristic thickness of the foam given by S_v^{-3} (which is proportional to D_m^3).

All the values of $\overline{g_v}$ available in the literature to our knowledge as well as ours are plotted as a function of ρ in Fig. 7. $\overline{g_v}$ for our structures appears to be nearly proportional with ρ. Such a dependence could be related to the range of studied ligament diameter. For instance Kwon et al. [40] show that $\overline{g_v}$ for NPG models can depend on the ligament diameter under certain conditions. However, it is also reported that experimental structures with different diameters are self-similar and that $\overline{g_v}$ does not depend on the ligament diameter [41]. Note that, the $\overline{g_v}$ values of the latter study are not included in Fig. 7 because their data are normalized by D_m^3 and not by S_v^{-3}.

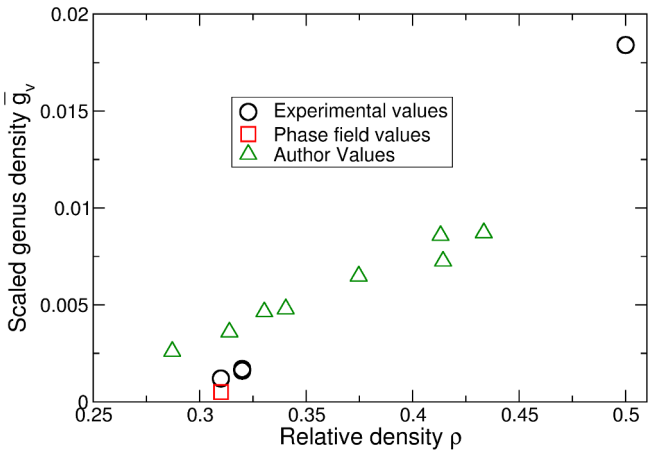

Fig. 7. Scaled genus density versus relative density. The black circles and red squares refer to values obtained with NPG samples [15,20,23] and phase field models [15], respectively. The green triangles correspond to our models.

There is a relatively fair agreement with other results except for $\rho = 0.5$. However the available data are rather scarce. The general trend is an increase of $\overline{g_v}$ as a function of ρ. This could be explained by considering that for two systems of equal D_m and V but with two different ρ values, the one with the lowest ρ will also have less ligaments, and hence a smaller genus. From a different but related point of view, decreasing the relative density should increase the aspect ratio of the ligaments to ensure percolation during the demixing. The aspect ratio being greater, the number of connections in the foam decreases.

The third quantity used to characterize the morphology is the interfacial shape distribution (ISD). The ISD is a representation of the two principal curvatures (κ_1 and κ_2) of a surface.

κ_1 and κ_2 are defined as the minimum and maximum normal curvatures of each discrete element of the surface. This concept can be illustrated by the special cases reported in Table 1. The ISD for one of our models is represented in Fig. 8. The comparison of this figure with those reported in the literature suggests that our models are in good agreement with experimental NPG [20,22,23].

Note that the atomistic model structures are generated using periodic boundary conditions but that the structural characterization is made within a finite volume. In order to evaluate the influence of non-periodic conditions, we increased the number of replicated volumes in all three directions and repeated the structural analysis. For instance, the Fig. 9 represents $\overline{g_v}$ for four different models as a function of the number of replicated volumes. Models with a small number of ligaments were deliberately chosen to enhance the finite size effect. One can see that the variations of $\overline{g_v}$ as a function of the number of replicated periodic volumes are much lower than those due to ρ. Nevertheless, this indicates that the influence of periodicity should be taken into account for structural analysis.

Table 1
Relations between principal curvatures and simple geometries. The "xor" logical operation is an exclusive "or".

$\kappa_1 = 0$ and $\kappa_2 = 0$	Plane
$\kappa_1 = 0$ xor $\kappa_2 = 0$	Cylinder
$\kappa_1 = \kappa_2$	Sphere
$\kappa_1 \times \kappa_2 > 0$	Ellipsoid
$\kappa_1 \times \kappa_2 < 0$	Hyperboloid

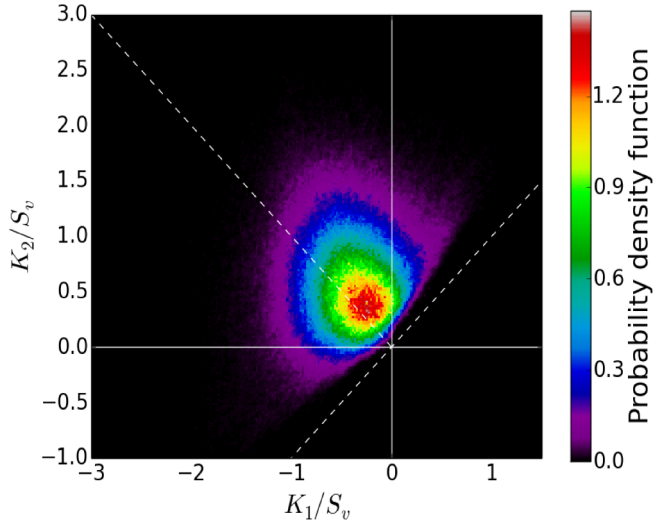

Fig. 8. Example of an interface shape distribution for one model foam ($S_v = 0.668$ nm^{-1}, $\rho = 0.43$, $D_m = 3.7$ nm).

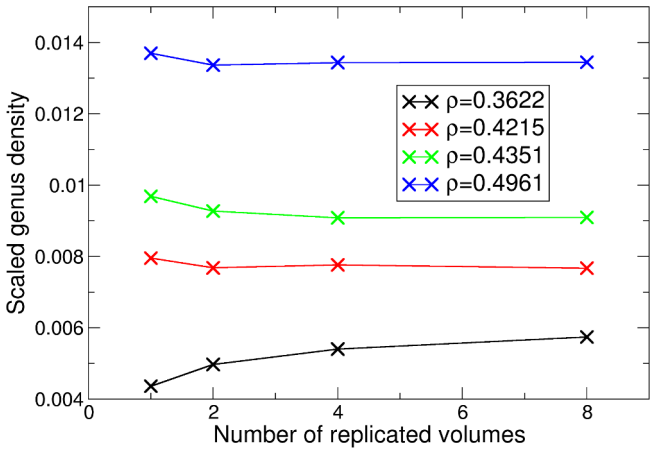

Fig. 9. Variation of the scaled genus density $\overline{g_v}$ as a function of the number of replicated volumes for four systems of different relative densities.

3.2. Mechanical properties

An example of tensile stress-strain curve is plotted in Fig. 10. Its shape closely resembles to other simulations results [9]. The difference with experimental curves [42] is discussed later in this section.

Using a linear regression between 0 and 2%, an elastic modulus E = 6.3 GPa is determined. A similar procedure is repeated for other systems, and values are reported in Fig. 11, with others from the literature. Our values are almostidentical in tension or in compression and are in the range of published data obtained by tensile deformation. However, they tend to be slightly lower than those obtained during compression. Dislocation analysis indicates that dislocations and stacking faults are present before any applied deformation. Those are nucleated during the relaxation of surface stresses. Hence, dislocations move at the very beginning of the test. This could explain the low moduli, although tests performed for quasi pristine structures do not lead to significantly higher values. These structures were obtained by relaxing the stresses at a lower temperature. The Fig. 11 also shows the Young modulus values predicted by the Gibson-Ashby model [43]. Most of the experimentally and theoretically reported data, including ours, appear to be lower. It was proposed that this difference may be due to a ligament size effect, with a bending mode contribution [9].

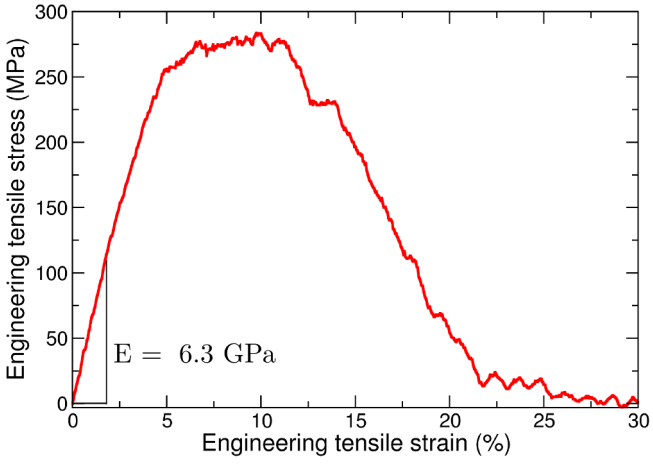

Fig. 10. Engineering stress versus engineering strain for the same system described in Figs. 6, 8, 12 and 13 ($\rho = 0.43$ and $D_m = 3.7$ nm).

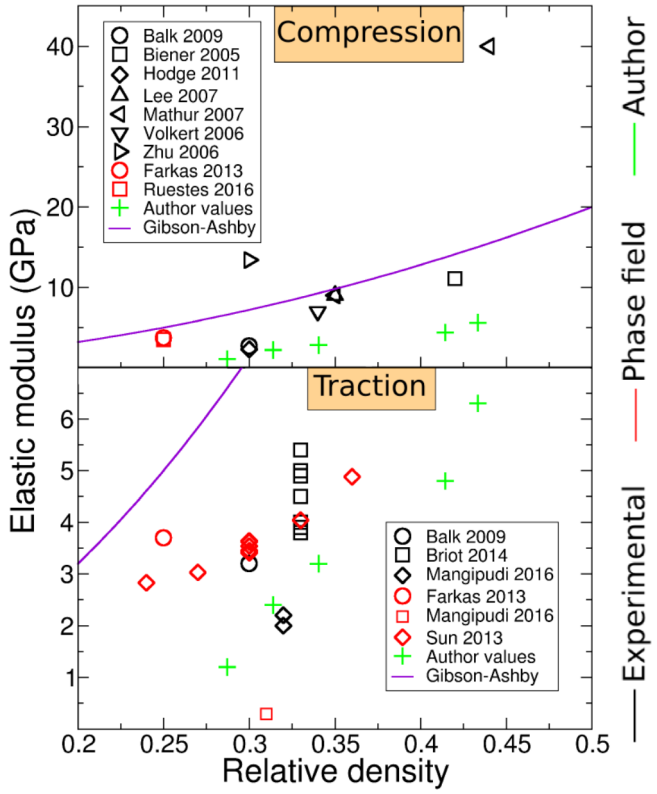

Fig. 11. Compilation of elastic moduli measured experimentally [12,15,42,44–49], computed for phase-field models [8,9,14,15] and for our systems (in black, red and green, respectively). Top graph: compression tests. Bottom graph: tensile tests. Purple curves show predictions from the Gibson-Ashby model [43] for a gold elastic modulus of 80 GPa.

The analysis of the tensile test corresponding to the Fig. 10 shows that before 10% strain, the ligaments are necking and after 10%, they are progressively breaking, leading to softening. Between 22% and 25% two unbroken ligaments remain (over $\simeq$ 25 involved in the fracture), and only one between 25% and 30%. The system is fully fractured for higher strain values.

NPG is brittle at the macroscopic scale although it has been shown that microscopically, ligaments are characterized by a significant elongation, necking and plasticity prior to failure [11,24,30,50]. It is commonly agreed that this behavior could be described by a random fuse model, where the rupture of weak ligaments will overload the surrounding ones, resulting in fast propagation of the crack through the nanoporous structure [11]. According to this model, a sufficiently narrow distribution is needed, otherwise the brittle character should be less pronounced [24].

Our simulations reproduce the ductile deformation of gold ligaments, as shown in Fig. 12. We observed that in the fracture plane most of the ligaments are stretched until a one or two-atoms thick wire remains. However, the stress (Fig. 10) does not fall abruptly as in experiments [12], rather suggesting an overall ductile failure of our NPG models. This issue is typical of molecular dynamics simulations of nanoporous systems [14]. The first explanation coming to mind is related to the size difference between the numerical and experimental samples. The former includes a small number of ligaments, that could impedes stress concentration, thus limiting fast crack propagation. This inherent limitation of molecular dynamics simulations seems difficult to overcome. Another source of discrepancy is the simulation time scale, dictating a very high strain rate in the mechanical tests. This also imposes a strong limitation on the amount of thermally activated plasticity mechanisms that could occur during the timespan of the simulations. Finally, there is a potential influence of the ligament diameter, which is

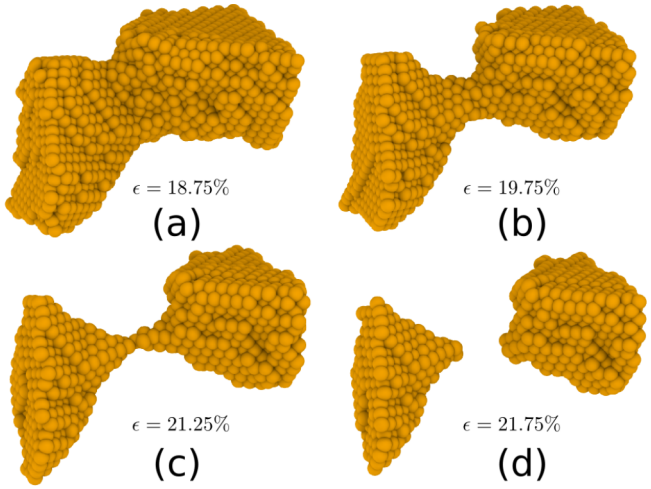

Fig. 12. Ligament necking (a–c) and breaking (c, d) during tensile test. The ligament shown here is extracted from the same foam than in Figs. 6, 8, 10, and 13.

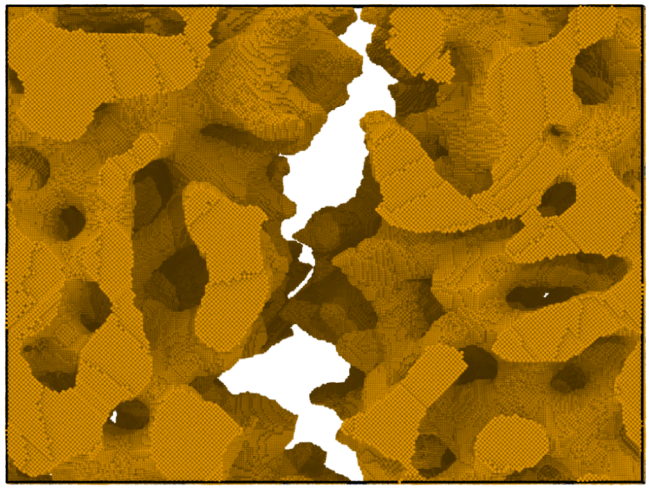

Fig. 13. Fractured system at 30% of strain. The fracture is localized in a plane, highlighting the correlation between the ligaments during the crack propagation.

lower in our systems than in experiments. For instance, in a recent work, it is suggested that very thin ligaments would promote ductility [24]. However, it is also mentioned that in these circumstances the sample fracture would result from uncorrelated ligament failure, leaving a rough fracture surface. It is then interesting and surprising to note that in our simulations, the fracture occurs in a well defined planar region, perpendicular to the deformation axis (Fig. 13), due to correlated ligament ruptures. This specific issue remains unanswered at the moment, stressing the need for further investigations.

4. Conclusions

In this paper, we describe an original method to generate NPG models by using only molecular dynamics, and perform a structural and mechanical characterization. Comparing our results with the literature shows that realistic foam structures can be generated with this approach. The method consists of demixing two liquid gold and silver phases during the MD simulations by using a repulsive Au-Ag interatomic potential, generating a bicontinuous structure. The gold liquid phase is replaced by a crystalline one, and the silver part is removed. This approach allows to generate models whose mean ligament

diameter and relative density can be precisely selected. Experimentally accessible ligament diameter can be obtained by running simulations of only a few 100 ps.

The structure of the models is analyzed by first determining the ligament diameter distributions. The scaled genus density is in agreement with previous results, and is found to increase, seemingly linearly, as a function of the relative density. Computed Interfacial shape distributions are also in good agreement with experiments. In order to characterize the mechanical behavior of our models, uniaxial tests in tension and in compression were performed. In tension, we found that the NPG fails by the successive rupture of several ligaments, localized in a planar region perpendicular to the deformation axis. Unlike in experiments, this process extends over a significant strain range, and is indicative of a ductile failure of the NPG. Finally, we calculated elastic moduli in both tension and compression, which are found to be in the range of data reported in the literature.

Data availability

The datasets generated and analysed during the current study are available from the corresponding author on reasonable request.

CRediT authorship contribution statement

Maxime Guillotte: Conceptualization, Methodology, Investigation, Writing - original draft. **Julien Godet:** Writing - review & editing, Supervision, Funding acquisition. **Laurent Pizzagalli:** Writing - review & editing, Supervision, Funding acquisition.

Acknowledgements

This work pertains to the French Government program Investissements d'Avenir (LABEX INTERACTIFS, reference ANR-11-LABX-0017-01). Computations have been performed on the supercomputer facilities of the Mésocentre de calcul Poitou-Charentes.

References

[1] Takeshi Fujita, Pengfei Guan, Keith McKenna, Xingyou Lang, Akihiko Hirata, Ling Zhang, Tomoharu Tokunaga, Shigeo Arai, Yuta Yamamoto, Nobuo Tanaka, Yoshifumi Ishikawa, Naoki Asao, Yoshinori Yamamoto, Jonah Erlebacher, Mingwei Chen, Atomic origins of the high catalytic activity of nanoporous gold, Nat. Mater. 11 (9) (September 2012) 775–780.

[2] Qin Wei, Yanfang Zhao, Xu. Caixia, Wu. Dan, Yanyan Cai, Jing He, He Li, Du. Bin, Minghui Yang, Nanoporous gold film based immunosensor for label-free detection of cancer biomarker, Biosens. Bioelectron. 26 (8) (April 2011) 3714–3718.

[3] L.Y. Chen, T. Fujita, M.W. Chen, Biofunctionalized nanoporous gold for electrochemical biosensors, Electrochim. Acta 67 (2012) 1–5.

[4] Erkin Seker, Yevgeny Berdichevsky, Matthew R. Begley, Michael L. Reed, Kevin J. Staley, Martin L. Yarmush, The fabrication of low-impedance nanoporous gold multiple-electrode arrays for neural electrophysiology studies, Nanotechnology 21 (12) (2010) 125504.

[5] Chuancheng Jia, Huiming Yin, Houyi Ma, Rongyue Wang, Xingbo Ge, Aiqiu Zhou, Xu. Xiaohong, Yi Ding, Enhanced photoelectrocatalytic activity of methanol oxidation on TiO_2-decorated nanoporous gold, J. Phys. Chem. C 113 (36) (2009) 16138–16143.

[6] Peter N. Ciesielski, Amanda M. Scott, Christopher J. Faulkner, Brad J. Berron, David E. Cliffel, G. Kane Jennings, Functionalized nanoporous gold leaf electrode films for the immobilization of photosystem I, ACS Nano 2 (12) (December 2008) 2465–2472.

[7] Hai-Jun Jin, Jörg Weissmüller, Diana Farkas, Mechanical response of nanoporous metals: a story of size, surface stress, and severed struts, MRS Bull. 43 (01) (January 2018) 35–42.

[8] Carlos J. Ruestes, Diana Farkas, Alfredo Caro, Eduardo M. Bringa, Hardening under compression in Au foams, Acta Mater. 108 (April 2016) 1–7.

[9] Xiao-Yu Sun, Xu. Guang-Kui, Xiaoyan Li, Xi-Qiao Feng, Huajian Gao, Mechanical properties and scaling laws of nanoporous gold, J. Appl. Phys. 113 (2) (January 2013) 023505 .

[10] Ling-Zhi Liu, Xing-Long Ye, Hai-Jun Jin, Interpreting anomalous low-strength and low-stiffness of nanoporous gold: quantification of network connectivity, Acta Mater. 118 (October 2016) 77–87.

[11] Juergen Biener, Andrea M. Hodge, Alex V. Hamza, Microscopic failure behavior of nanoporous gold, Appl. Phys. Lett. 87 (12) (September 2005) 121908 .

[12] Nicolas J. Briot, Tobias Kennerknecht, Christoph Eberl, T. John Balk, Mechanical properties of bulk single crystalline nanoporous gold investigated by millimetre-scale tension and compression testing, Philos. Mag. 94 (8) (2014) 847–866.

[13] Carlos J. Ruestes, Daniel Schwen, Emmanuel N. Milln, Emiliano Aparicio, Eduardo M. Bringa, Mechanical properties of Au foams under nanoindentation, Comput. Mater. Sci. 147 (May 2018) 154–167.

[14] Diana Farkas, Alfredo Caro, Eduardo Bringa, Douglas Crowson, Mechanical response of nanoporous gold, Acta Mater. 61 (9) (May 2013) 3249–3256.

[15] K.R. Mangipudi, E. Epler, C.A. Volkert, Topology-dependent scaling laws for the stiffness and strength of nanoporous gold, Acta Mater. 119 (October 2016) 115–122.

[16] Bao-Nam Dinh Ngô, Alexander Stukowski, Nadiia Mameka, Jürgen Markmann, Karsten Albe, Jörg Weissmüller, Anomalous compliance and early yielding of nanoporous gold, Acta Mater. 93 (2015) 144–155.

[17] B.-N.D. Ngô, B. Roschning, K. Albe, J. Weissmüller, J. Markmann, On the origin of the anomalous compliance of dealloying-derived nanoporous gold, Scr. Mater. 130 (March 2017) 74–77.

[18] O. Zinchenko, H.A. De Raedt, E. Detsi, P.R. Onck, J.T.M. De Hosson, Nanoporous gold formation by dealloying: a Metropolis Monte Carlo study, Comput. Phys. Commun. 184 (6) (June 2013) 1562–1569.

[19] Lijie He, Niaz Abdolrahim, Deformation mechanisms and ductility enhancement in core-shell Cu@Ni nanoporous metals, Comput. Mater. Sci. 150 (July 2018) 397–404.

[20] K.R. Mangipudi, V. Radisch, L. Holzer, C.A. Volkert, A FIB-nanotomography method for accurate 3d reconstruction of open nanoporous structures, Ultramicroscopy 163 (April 2016) 38–47.

[21] H. Rösner, S. Parida, D. Kramer, C.A. Volkert, J. Weissmüller, Reconstructing a nanoporous metal in three dimensions: an electron tomography study of dealloyed gold leaf, Adv. Eng. Mater. 9 (7) (July 2007) 535–541.

[22] Yu-chen Karen Chen-Wiegart, Steve Wang, Yong S. Chu, Wenjun Liu, Ian McNulty, Peter W. Voorhees, David C. Dunand. Structural evolution of nanoporous gold during thermal coarsening, Acta Mater. 60 (12) (2012) 4972–4981.

[23] Yu-chen Karen Chen, Yong S. Chu, JaeMock Yi, Ian McNulty, Qun Shen, Peter W. Voorhees, David C. Dunand, Morphological and topological analysis of coarsened nanoporous gold by x-ray nanotomography, Appl. Phys. Lett. 96 (4) (January 2010) 043122 .

[24] Nilesh Badwe, Xiying Chen, Karl Sieradzki, Mechanical properties of nanoporous gold in tension, Acta Mater. 129 (May 2017) 251–258.

[25] Steve Plimpton, Fast parallel algorithms for short-range molecular dynamics, J. Comput. Phys. 117 (1995) 1–19.

[26] Alexander Stukowski, Visualization and analysis of atomistic simulation data with Ovito-the open visualization tool, Modell. Simul. Mater. Sci. Eng. 18 (1) (January 2010) 015012 .

[27] S.M. Foiles, M.I. Baskes, M.S. Daw, Embedded-atom-method functions for the fcc metals Cu, Ag, Au, Ni, Pd, Pt, and their alloys, Phys. Rev. B 33 (12) (June 1986) 7983–7991.

[28] Alexander Stukowski, Computational analysis methods in atomistic modeling of crystals, JOM 66 (3) (March 2014) 399–407.

[29] A. Prakash, M. Hummel, S. Schmauder, E. Bitzek, Nanosculpt: a methodology for generating complex realistic configurations for atomistic simulations, MethodsX 3 (2016) 219–230.

[30] N.A. Senior, R.C. Newman, Synthesis of tough nanoporous metals by controlled electrolytic dealloying, Nanotechnology 17 (9) (May 2006) 2311–2316.

[31] Steven Van Petegem, Stefan Brandstetter, Robert Maass, Andrea M. Hodge, Bassem S. El-Dasher, Jürgen Biener, Bernd Schmitt, Camelia Borca, Helena Van Swygenhoven, On the microstructure of nanoporous gold: an X-ray diffraction study, Nano Lett. 9 (3) (March 2009) 1158–1163.

[32] S. Parida, D. Kramer, C.A. Volkert, H. Rösner, J. Erlebacher, J. Weissmüller, Volume change during the formation of nanoporous gold by dealloying, Phys. Rev. Lett. 97 (3) (July 2006).

[33] L.H. Qian, M.W. Chen, Ultrafine nanoporous gold by low-temperature dealloying and kinetics of nanopore formation, Appl. Phys. Lett. 91 (8) (August 2007) 083105 .

[34] Zhonghua Zhang, Chi Zhang, Yulai Gao, Jan Frenzel, Junzhe Sun, Gunther Eggeler, Dealloying strategy to fabricate ultrafine nanoporous gold-based alloys with high structural stability and tunable magnetic properties, CrystEngComm 14 (23) (2012) 8292.

[35] Lihua Qian, Wen Shen, Biswajit Das, Bo Shen, Gaowu W. Qin, Alumina coating of ultrafine nanoporous gold at room temperature and their optical properties, Chem. Phys. Lett. 479 (4–6) (September 2009) 259–263.

[36] Zhonghua Zhang, Yan Wang, Yingzi Wang, Xiaoguang Wang, Zhen Qi, Hong Ji, Changchun Zhao, Formation of ultrafine nanoporous gold related to surface diffusion of gold adatoms during dealloying of Al_2Au in an alkaline solution, Scr. Mater. 62 (3) (February 2010) 137–140.

[37] Takeshi Fujita, Li-Hua Qian, Koji Inoke, Jonah Erlebacher, Ming-Wei Chen, Three-dimensional morphology of nanoporous gold, Appl. Phys. Lett. 92 (25) (June 2008) 251902 .

[38] C. Min Ma, Milan Sonka, A fully parallel 3d thinning algorithm and its applications, Comput. Vis. Image Underst. 64 (3) (November 1996) 420–433.

[39] Y. F Tsao, K. S Fu, A parallel thinning algorithm for 3-D pictures, Comput. Graphics Image Process. 17 (4) (December 1981) 315–331.

[40] Y. Kwon, K. Thornton, P.W. Voorhees, The topology and morphology of bicontinuous interfaces during coarsening, Europhys. Lett. 86 (4) (May 2009) 46005.

[41] Hu. Kaixiong, Markus Ziehmer, Ke Wang, Erica T. Lilleodden, Nanoporous gold: 3d structural analyses of representative volumes and their implications on scaling relations of mechanical behaviour, Philos. Mag. 96 (32–34) (2016) 3322–3335.

[42] T. John Balk, Chris Eberl, Ye Sun, Kevin J. Hemker, Daniel S. Gianola. Tensile,

compressive microspecimen testing of bulk nanoporous gold, JOM 61 (12) (2009) 26–31.
[43] L.J. Gibson, M.F. Ashby (Eds.), Cellular Solids: Structure and Properties. Cambridge Solid State Science Series, Cambridge University Press, Cambridge, 1997.
[44] Juergen Biener, Andrea M. Hodge, Alex V. Hamza, Luke M. Hsiung, Joe H. Satcher, Nanoporous Au: a high yield strength material, J. Appl. Phys. 97 (2) (January 2005) 024301 .
[45] A.M. Hodge, R.T. Doucette, M.M. Biener, J. Biener, O. Cervantes, A.V. Hamza, Ag effects on the elastic modulus values of nanoporous Au foams, J. Mater. Res. 24 (04) (April 2009) 1600–1606.
[46] Dongyun Lee, Xiaoding Wei, Xi Chen, Manhong Zhao, Seong.C. Jun, James Hone, Erik G. Herbert, Warren C. Oliver, Jeffrey W. Kysar, Microfabrication and mechanical properties of nanoporous gold at the nanoscale, Scr. Mater. 56 (5) (2007) 437–440.
[47] Anant Mathur, Jonah Erlebacher, Size dependence of effective Young's modulus of nanoporous gold, Appl. Phys. Lett. 90 (6) (February 2007) 061910 .
[48] C.A. Volkert, E.T. Lilleodden, D. Kramer, J. Weissmüller, Approaching the theoretical strength in nanoporous Au, Appl. Phys. Lett. 89 (6) (August 2006) 061920 .
[49] Jianzhong Zhu, Erkin Seker, Hilary Bart-Smith, Matthew R. Begley, Robert G. Kelly, Giovanni Zangari, Whye-Kei Lye, Michael L. Reed, Mitigation of tensile failure in released nanoporous metal microstructures via thermal treatment, Appl. Phys. Lett. 89 (13) (September 2006) 133104 .
[50] Rong Li, K. Sieradzki, Ductile-brittle transition in random porous Au, Phys. Rev. Lett. 68 (8) (1992) 1168–1171.